Structural and magnetic properties of non-stoichiometric $Fe_2Zr$



2007 J. Phys.: Condens. Matter 19 376202

(http://iopscience.iop.org/0953-8984/19/37/376202)

IOP PUBLISHING JOURNAL OF PHYSICS: CONDENSED MATTER

J. Phys.: Condens. Matter **19** (2007) 376202 (8pp) doi:10.1088/0953-8984/19/37/376202

# Structural and magnetic properties of non-stoichiometric $Fe_2Zr$

**N Mattern[1], W X Zhang[1], S Roth[1], H Reuther[2], C Baehtz[2,3] and M Richter[1]**

[1] Leibniz-Institut für Festkörper- und Werkstoffforschung IFW Dresden, Helmholtzstraße 20, D-01069 Dresden, Germany
[2] Forschungszentrum Dresden-Rossendorf, Postfach 51 01 19, D-01314 Dresden, Germany
[3] Hasylab at Desy, Notke Straße 85, D-22603 Hamburg, Germany

E-mail: n.mattern@ifw-dresden.de

Received 25 June 2007, in final form 19 July 2007
Published 22 August 2007
Online at stacks.iop.org/JPhysCM/19/376202

**Abstract**

The lattice parameters and magnetic properties of the C15 Laves phase $Fe_2Zr$ vary systematically within the homogeneity range of the compound from 66.7 at.% to 74.5 at.% Fe. In the non-stoichiometric compounds Zr is partly substituted by the excess Fe. The magnetic moment per iron atom increases with the Fe content. Electronic structure calculations show an enhanced magnetic moment of the excess Fe at the Zr site, which explains well the composition dependence.

## 1. Introduction

The magnetic properties of inter-metallic Laves phases $A_2B$ depend strongly on the kind of atoms, where A is a magnetic transition metal like Fe, Co, Ni, Mn and B is Zr, Ti, Hf, Sc, Y, or a rare-earth atom. For example, giant room temperature magnetostriction occurs in $Fe_2Tb$ and $Fe_2Dy$ [1], large magnetovolume effects leading to Invar-like behavior were also observed in $Fe_2Zr$, $Fe_2Hf$, and $Fe_2Sc$ [2], and a first order magnetic transition at about 60 K is found in doped $Fe_2Ce$ [3]. The magnetic properties can be changed by atomic substitution [4–6], or by introduction of non-metals like hydrogen [7] or boron [8]. On the other hand, binary Laves phases possess a homogeneity range, which gives the reason for a range of properties. Substitutional anti-site defects are present in non-stoichiometric $Co_2Zr$ alloys [9]. The presence of a homogeneity range of the $Fe_2Zr$ Laves phase was already pointed out 40 years ago [10, 11]. Then, a certain scatter in the properties was reported, caused by uncertainties in composition. Recent reports on the binary Fe–Zr phase diagram also exhibit discrepancies with respect to the phases formed as well as to the extension of homogeneity ranges [12–15].

The crystal structure and magnetization density of single crystalline $Fe_2Zr$ was determined by means of neutron scattering at 4 K [16]. $Fe_2Zr$ crystallizes in the cubic C15 Laves phase with the space group $Fd\bar{3}m$. The Fe atoms are situated at 16(d) sites (I), and the Zr atoms

**Table 1.** Structural properties of $Fe_xZr_{100-x}$ at room temperature (lattice parameter $a_0$, occupancy O of $Fe^{II}$ at Zr site 8(a), mass density $\sigma_m$, x-ray density $\sigma_x$).

| Alloy | Fe (at.%) Zr (at.%) | Phases $x$ (vol%) | $a_0$ (nm) Experimental | $a_0$ (nm) Theoretical | O | $\sigma_m$ (g cm$^{-3}$) | $\sigma_x$ (g cm$^{-3}$) |
|---|---|---|---|---|---|---|---|
| $Fe_{67}Zr_{33}$ | 66.85<br>33.15 | $Fe_2Zr$ (99)<br>$Fe_{23}Zr_6$ (1) | 0.707 57<br>— | 0.6850 | 0.0 | 7.511 | 7.608 |
| $Fe_{70}Zr_{30}$ | 70.05<br>29.95 | $Fe_2Zr$ (99)<br>$Fe_{23}Zr_6$ (1) | 0.705 70<br>— | 0.6825 | 0.08 | 7.513 | 7.555 |
| $Fe_{72}Zr_{28}$ | 71.98<br>28.02 | $Fe_2Zr$ (97)<br>$Fe_{23}Zr_6$ (1)<br>Fe (2) | 0.703 42<br>— | 0.6770 | 0.15 | 7.527 | 7.529 |
| $Fe_{79}Zr_{21}$ | 78.86<br>21.14 | $Fe_2Zr$ (79)<br>$Fe_{23}Zr_6$ (4)<br>Fe (16) | 0.701 14<br>1.170 2<br>0.286 6 | 0.6763 | 0.18 | 7.588 | 7.570 |

occupy the 8(a) sites (II). The aim of this work was to analyze the structure–property relation of the $Fe_2Zr$ Laves phase as a function of the Fe content.

## 2. Experimental and theoretical details

Ingots of the nominal alloys $Fe_xZr_{100-x}$ ($x = 66.7, 70.0, 72.0, 79.0$) were melted from elements Fe and Zr (Alfa Aesar) in an argon arc furnace, using a non-consumable tungsten electrode on a water-cooled copper hearth. The mass of each ingot was about 50 g. The ingots were wrapped in tantalum foil, annealed at 1200 °C for 24 h in sealed silica ampoules under 15 kPa purified Ar gas and then quenched in water. Pieces were cut electro-erosively for the measurement of the magnetic properties. Powder samples were prepared for x-ray diffraction (XRD) by ball milling in a Fritsch Pulverisette. Sieved material (<100 $\mu$m) was filled under helium atmosphere into a capillary, which was sealed afterwards. The XRD patterns were recorded at different temperatures in Debye–Scherrer geometry at the powder diffraction line B2 of the synchrotron HASYLAB. The experimental set-up (wavelength $\lambda = 0.069\,95$ nm) consists of a furnace and an image plate detector system [17]. Chemical analysis was performed independently for iron and zirconium by a titration technique combined with optical emission spectrometry. The magnetization loops were measured at 5 and 300 K with the SQUID magnetometer MPMS-7XL (Quantum Design) in a field range from $-5$ to $+5$ T. A home-built Faraday magnetometer was used to obtain magnetization–temperature curves from 300 K up to 1073 K in a field of $\mu_0 H = 0.58$ T.

Density functional calculations were carried out with the full potential local orbital code, FPLO5.00-18 [18]. Chemical disorder was treated by the coherent potential approximation (CPA) [19]. The valence basis sets comprised 3s3p/3d4s4p states for iron and 3d4s4p/4d5s5p states for zirconium. The local spin density approximation (LSDA) in the parameterization of Perdew and Wang 92 [20] was used in all calculations. The number of $k$ points in the irreducible wedge of the Brillouin zone was set to 196. Energy convergence at the level of $10^{-7}$ Hartree was achieved during the self-consistent iterations.

## 3. Results and discussion

The chemical compositions of the alloys given in table 1 (at.%) are in good agreement with the nominal values. Figure 1 shows the corresponding XRD patterns of the $Fe_xZr_{100-x}$ alloys. For

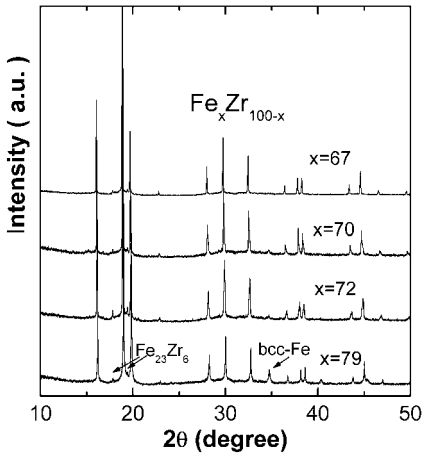


**Figure 1.** XRD patterns of $Fe_xZr_{100-x}$ at room temperature.

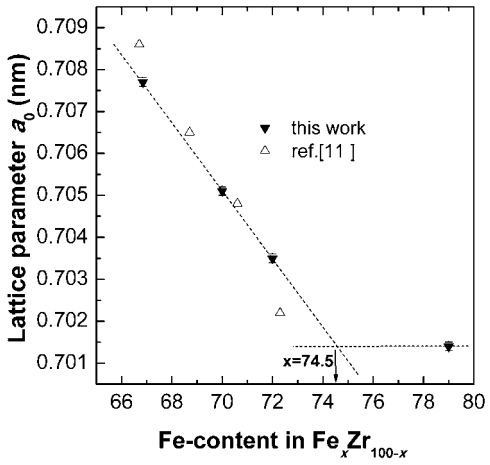


**Figure 2.** Dependence of the lattice parameter $a_0$ of the $Fe_2Zr$ phase on the Fe content of the ingot.

the alloys with $x = 66.7$, 70, and 72, the cubic C15 Laves phase $Fe_2Zr$ is observed with traces of bcc Fe and for $x = 72$ also with a trace of the cubic $Fe_{23}Zr_6$ phase. The $x = 79$ alloy consists of a phase mixture of $Fe_2Zr$, bcc Fe and $Fe_{23}Zr_6$. The diffraction patterns were analyzed by a multiphase Rietveld refinement [21]. The obtained structural parameters are summarized in table 1. Figure 2 shows the behavior of the lattice parameter $a_0$ of the $Fe_2Zr$ phase as a function of the chemical composition of the alloy. A linear decrease of $a_0$ with increasing Fe content is observed in agreement with earlier literature data [10] which are also given in figure 2. From the composition dependence of the lattice parameter the iron-rich phase boundary of $Fe_2Zr$ at 1200 °C is estimated to $x = 74.5$. The fit of the site occupations indicates substitutional disorder. In the non-stoichiometric compounds the excess Fe atoms are situated at the 8(a) $Zr^{II}$ sites, while an occupation of 16(d) sites by Zr is below the experimental accuracy. The values of the site occupancy obtained by Rietveld refinement are given in table 1. The substitution of Zr atoms by Fe in the non-stoichiometric compounds is also confirmed by the comparison of the experimental mass densities with the calculated x-ray densities as given in table 1.

The temperature dependences of the lattice parameters were determined by *in situ* x-ray diffraction measurements at elevated temperatures. Figure 3 shows the lattice expansion of the C15 Laves phase for the different alloy compositions. Above $T = 550$ °C, a linear dependence

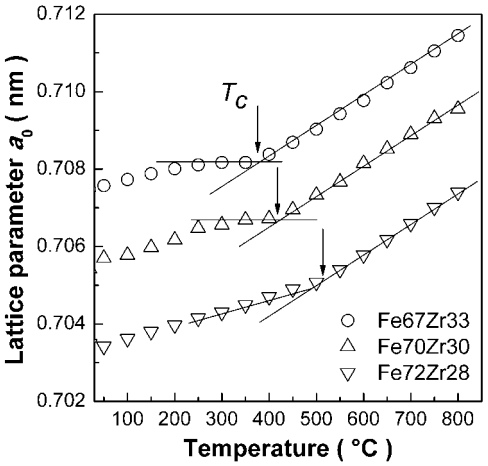


**Figure 3.** Lattice parameters $a_0$ of $Fe_xZr_{100-x}$ versus temperature.

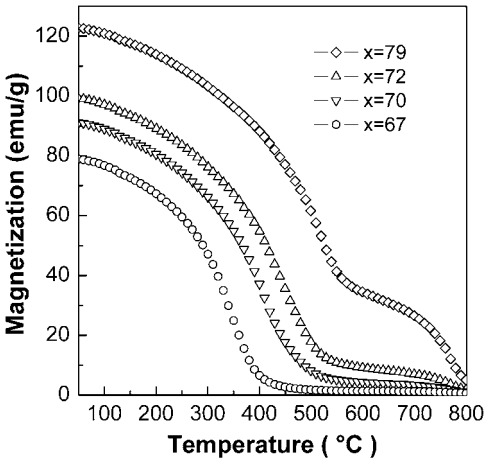


**Figure 4.** Magnetization of $Fe_xZr_{100-x}$ versus temperature at $\mu_0 H = 0.58$ T.

**Table 2.** Magnetic properties of $Fe_xZr_{100-x}$ (Curie temperature $T_C$, magnetic moment per iron atom $m$, saturation magnetostriction $\lambda_{Ms}$, fraction of bcc Fe).

| Alloy | $T_c$ (°C) | $m_{T=5\ K}$ ($\mu_B$) | $m_{T=300\ K}$ ($\mu_B$) | $\lambda_{Ms}$ (ppm) | $x$ (vol%) |
|---|---|---|---|---|---|
| $Fe_{67}Zr_{33}$ | 356 | 1.670 | 1.42 | 17 | 0.5 |
| $Fe_{70}Zr_{30}$ | 427 | 1.765 | 1.548 | 14 | 1 |
| $Fe_{72}Zr_{28}$ | 466 | 1.823 | 1.59 | 10 | 3 |
| $Fe_{79}Zr_{21}$ | 548 | 1.876 | 1.65 | 8 | 19 |

of $a_0$ on temperature is observed with an expansion coefficient $\alpha = 12 \times 10^{-6}$ K$^{-1}$. Below temperatures $T$ around 500 °C, the thermal expansion exhibits an anomalous behavior which is related to the magnetic phase transition. Figure 4 shows the corresponding temperature dependence of the magnetization curves $M(T)$. The magnetic transition of the ferromagnetic $Fe_xZr_{100-x}$ phase into the paramagnetic state occurs between 350 and 500 °C depending on the Fe content. At higher temperature, $T > 500$ °C, the non-zero magnetization indicates the presence of the second phase bcc Fe in the sample. From the value of the magnetization at $T = 600$ °C the volume fraction of bcc Fe was estimated. The corresponding data are given in table 2. They are found to be comparable with those of the XRD results. The

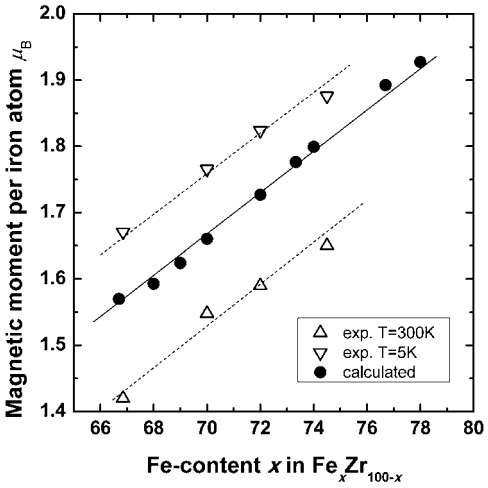


**Figure 5.** Magnetic moment of the C15 phase versus Fe content in $\mu_B$ per Fe atom.

Curie temperature $T_C$ of the $Fe_2Zr$ phase was calculated by the intercept of $M^{1.7}(T)$ versus temperature $T$. The values are given in table 2, and also indicated by the arrows in figure 3. The Curie temperature increases monotonically with the Fe content of the C15 $Fe_2Zr$ phase. The deviation of the thermal expansion from the linear behavior below $T_C$ (figure 3) is the well-known Invar effect. The spontaneous magnetostriction in the ferromagnetic state provides an additional contribution to the volume. Therefore, the thermal expansion consists of a structural and a magnetic contribution, i.e., $V(T) = V_G(T) + V_M(T)$. At temperatures below $T_C$ the magnetic part is $V_M \sim [(M_s(T))]^2$, and at temperatures above $T_C$ it vanishes [5].

The saturation magnetization $M_s$ of the alloys was determined by the measurement of the magnetization versus applied magnetic field $M(H)$ at two temperatures, $T = 5$, and 300 K. From the values of $M_s$ the magnetic moment per Fe atom was calculated. To subtract the contribution of the Zr atoms, a value of $-0.34$ $\mu_B$ per Zr atom was used [16]. A somewhat higher value of about $-0.5$ $\mu_B$ per Zr atom was obtained in our LSDA calculation, see below. Further, the contribution of the bcc Fe phase was subtracted for the calculation of the magnetic moment by taking the corresponding volume fractions into account. Figure 5 shows a comparison between experimental magnetic moments per iron atom as a function of composition with results from our LSDA calculations at the theoretical lattice constant. The increased Fe content enlarges the magnetic moment per iron atom of the $Fe_2Zr$ phase up to 0.2 $\mu_B$, where the dependence on $x$ is almost linear. Experimental and theoretical data show the same slope.

The magnetic properties of the $Fe_2Zr$ alloys were further analyzed by conversion electron Mößbauer (CEM) spectroscopy at room temperature. Figure 6 shows the corresponding Mößbauer patterns. As expected for the magnetically ordered state we observe magnetic six-line patterns. The crystallographically equivalent Fe sites can experience inequivalent magnetic fields due to different dipole contributions depending on the alignment of the magnetic moments [22]. Therefore, the CEM spectra which are split into two components, were fitted by two sextets with a fixed intensity ratio of 1:3. This accounts for an assumed moment alignment along [111]; see [23]. The line intensity ratios of the sextets differ from those of a randomly polycrystalline material due to texture by the large grain size in the annealed bulk samples. The hyperfine parameters calculated from the spectrum fits are summarized in table 3. For the alloy $Fe_{72}Zr_{28}$, a third sextet is observed corresponding to the presence of Fe atoms with a higher value of the hyperfine field. The hyperfine fields $B_{hf}$ of both sextets of the $Fe_2Zr$ phase

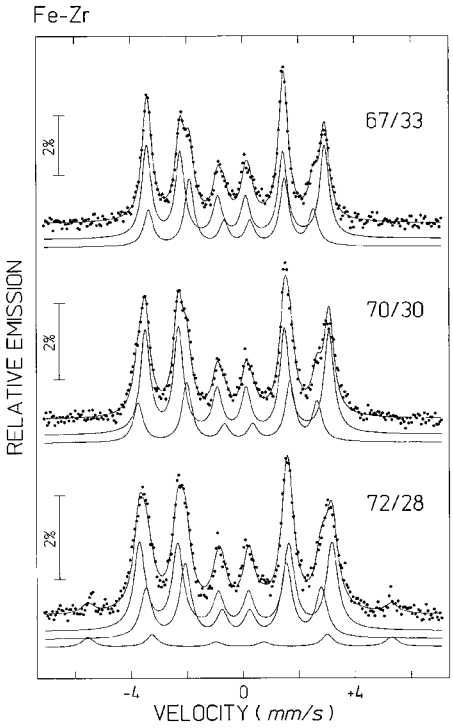


**Figure 6.** Mößbauer spectra of $Fe_xZr_{100-x}$ obtained at room temperature.

**Table 3.** Parameters of the Mößbauer CEM spectra at room temperature ($\delta$: isomer shift, $\Delta$: quadrupole splitting, $B_{hf}$: magnetic hyperfine field, $\lambda$: linewidth (same for all subspectra)).

| Alloy | Fe site | $\delta$ (mm s$^{-1}$) | $\Delta$ (mm s$^{-1}$) | $B_{hf}$ (T) | $\lambda$ (mm s$^{-1}$) | Area (%) |
|---|---|---|---|---|---|---|
| $Fe_{67}Zr_{33}$ | 1 | −0.201 | 0.119 | 19.6 | 0.452 | 75 |
| | 2 | −0.174 | −0.253 | 18.1 | | 25 |
| $Fe_{70}Zr_{30}$ | 1 | −0.193 | 0.114 | 20.6 | 0.470 | 75 |
| | 2 | −0.190 | −0.174 | 18.8 | | 25 |
| $Fe_{72}Zr_{28}$ | 1 | −0.194 | 0.075 | 21.0 | 0.506 | 70.1 |
| | 2 | −0.200 | −0.124 | 19.1 | | 23.4 |
| | 3 | −0.047 | 0 | 33.5 | | 6.5 |

increase with increasing Fe content due to the changes in the local environment of the iron atoms.

In order to understand the compounds from a microscopic point of view we performed electronic structure calculations. Guided by the experimental information, we assumed excess Fe atoms to occupy exclusively the 8(a) positions. The lattice parameter was varied for each composition in order to obtain the corresponding ground state with the lowest total energy. The decrease of the lattice constant $a_0$ as a function of the iron content in the experiments is reproduced by the calculations (table 1). The lattice constants themselves are about 3% smaller compared with the experimental ones, which is within the usual limit of the LSDA.

In the stoichiometric compound $Fe_2Zr$, the calculated moments amount to 1.65 $\mu_B$ for $Fe^I$ atoms at 16(d) sites and to $-0.50$ $\mu_B$ for the $Zr^{II}$ atoms at 8(a) sites, respectively. In the

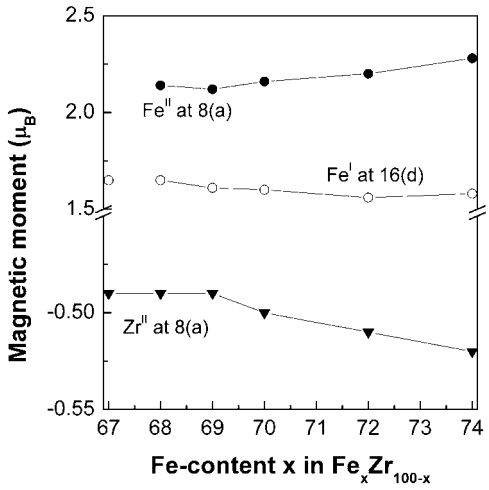


**Figure 7.** Calculated magnetic moments per atom at 16(d) (I) and 8a (II) lattice sites of the C15 structure versus Fe content.

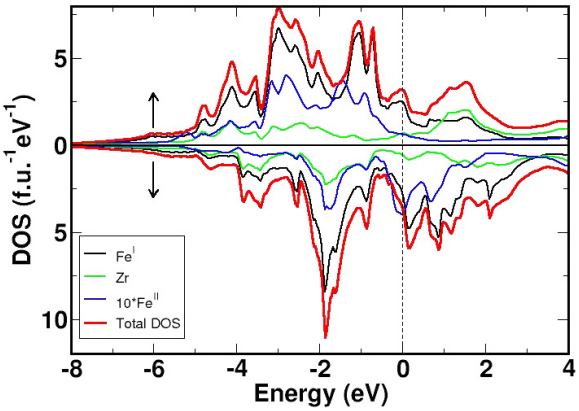


**Figure 8.** Total and site resolved spin densities of states of non-stoichiometric $Fe_{70}Zr_{30}$. The lattice parameter $a_0$ is 0.6825 nm.

(This figure is in colour only in the electronic version)

non-stoichiometric compounds, the excess $Fe^{II}$ atoms at the 8(a) sites exhibit an enhanced magnetic moment which increases further with the Fe content as shown in figure 7. The magnetic moment of $Fe^{II}$ is close to that of bcc Fe ($\sim$2.2 $\mu_B$). The related site resolved spin densities of states (DOS) show the characteristics of strong ferromagnetism (fully occupied majority spin subband; see figure 8) for $Fe^{II}$, while $Fe^{I}$ is weakly ferromagnetic with an incompletely occupied majority spin subband. The nearest neighbor of Zr in the C15 phase is $Fe^{I}$ and the second nearest neighbor is the doped $Fe^{II}$. This leads to a stronger hybridization between the non-magnetic Zr and $Fe^{I}$ than between Zr and $Fe^{II}$, which is visible in the DOS shown in figure 8. Moreover, the nearest neighbors of the doped $Fe^{II}$ atoms are $Fe^{I}$ atoms with a distance larger than the distance between $Fe^{I}$ and neighboring $Fe^{I}$. Thus the atomic volume of $Fe^{II}$ is larger than that of $Fe^{I}$ and the related bands are narrower. Both facts provide a reason for the larger moment on the $Fe^{II}$ sites in comparison with the $Fe^{I}$ sites; figure 7.

The averaged total magnetic moments per iron atom calculated at the respective experimental lattice constants are shown in figure 5 in comparison with the data measured at 5 K and room temperature. The deviations in the absolute values are within 5% and the LSDA underestimates the magnetic moment. About half of this difference can be attributed to the neglect of the orbital moments in the present scalar relativistic calculations. The linear composition dependence of the magnetic moment is in a good agreement with the experimental data showing almost the same derivative.

## 4. Conclusions

The C15 Laves phase $Fe_2Zr$ exhibits a homogeneity range from 66.7 at.% to 74.5 at.% Fe. The crystal structure parameter and the magnetic properties change systematically with the composition. In the non-stoichiometric compounds Zr atoms are partly substituted by the excess Fe atoms. The magnetic moment per iron atom of the $Fe_2Zr$ phase increases with the Fe content. Calculations of the electronic structure for non-stoichiometric $Fe_2Zr$ show an enhanced magnetic moment of the excess Fe atoms at the Zr site, which well explains the composition dependence.

## Acknowledgments

The authors thank M Frey for sample preparation and B Opitz for technical support. Financial support of the Deutsche Forschungsgemeinschaft DFG (project Ma1531/5) and from DAAD (WZ) is gratefully acknowledged.

## References

[1] Clark A E and Belson H S 1972 *Phys. Rev.* B **5** 3642
[2] Muraoka Y, Shiga M and Nakamura Y 1976 *J. Phys. Soc. Japan* **40** 905
[3] Roy S B, Perkins G K, Chattopadhyay M K, Nigam A K, Sokhey K J S, Chaddah P, Chaplin A D and Cohen L F 2004 *Phys. Rev. Lett.* **92** 147203
[4] Buschow K H J and Stapele R P 1970 *J. Appl. Phys.* **41** 4066
[5] Muraoka Y, Shiga M and Nakamura Y 1980 *J. Phys. F: Met. Phys.* **10** 127
[6] Gabay A M and Gaviko V S 2003 *J. Magn. Magn. Mater.* **260** 425
[7] Paul-Boncour V 2004 *J. Alloys Compounds* **367** 185
[8] Ren W J, Zhang Z D, Liu J P, Zhao X G, Liu W, Geng D Y and Jin X M 2002 *J. Appl. Phys.* **91** 8207
[9] Zhu J H and Liu C T 2000 *Acta Mater.* **48** 2339
[10] Brückner W, Kleinstück K and Schulze G E R 1967 *Phys. Status Solidi* **2** 475
[11] Brückner W, Pertel R, Kleinstück K and Schulze G E R 1968 *Phys. Status Solidi* **29** 211
[12] Okamato H 1993 *J. Phase Equilib.* **14** 652
[13] Servant C, Gueneau C and Ansara I 1995 *J. Alloys Compounds* **220** 19
[14] Jiang M, Oikawa K, Ikeshoji T, Wulff L and Ishida K 2001 *J. Phase Equilib.* **22** 406
[15] Stein F, Sauthoff G and Palm M 2002 *J. Phase Equilib.* **23** 480
[16] Warren P, Forsyth J B, McIntyre G J and Bernhoeft N 1992 *J. Phys.: Condens. Matter* **4** 5795
[17] Knapp M, Joco V, Bähtz C, Brecht H H, Berghäuser A, Ehrenberg H, von Seggern H and Fuess H 2004 *Nucl. Instrum. Methods* A **521** 565
[18] Koepernik K and Eschrig H 1999 *Phys. Rev.* B **59** 1743 http://www.fplo.de/
[19] Koepernik K, Velický B, Hayn R and Eschrig H 1997 *Phys. Rev.* B **55** 5717
[20] Perdew J P and Wang Y 1992 *Phys. Rev.* B **45** 13244
[21] Young R A 1993 *The Rietveld Method* (*Intern. Union of Crystallography*) (Oxford: Oxford University Press) pp 1–298
[22] Bowden G J 1973 *J. Phys. F: Met. Phys.* **3** 2206
[23] Wiesinger G, Oppelt A and Buschow K H J 1981 *J. Magn. Magn. Mater.* **22** 227